AIAA JOURNAL
Vol. 35, No. 5, May 1997

Balance Technique for Monitoring In Situ Structural Integrity of Prismatic Structures

Kara J. Peters* and Peter D. Washabaugh†
University of Michigan, Ann Arbor, Michigan 48109-2118

A general method to monitor the structural integrity of prismatic structures composed of simple isotropic linear elastic materials is described and justified by a detailed mathematical model. This technique is distinct from usual approaches in that a small number of distributed sensors is shown to be sensitive to the presence of damage throughout the entire volume of a structure without determining its location. In addition, this approach inherently operates as a binary sensor, thus alleviating the need to collect a large amount of data. Potential extensions to more general structural geometries and materials also are described.

I. Introduction

MANY approaches to monitoring structural integrity, such as ultrasonic, acoustic emission, or x-ray techniques, usually require extensive equipment and postprocessing of data, which inhibits their use as a real-time or in situ monitoring method.[1] In other words, equipment and data requirements of many measurement techniques typically preclude or limit their use in everyday aerospace systems. Thus, studies have been performed that can take a limited amount of spatial and temporal information and "invert" or determine the state of a structure.[2–4] In addition, such approaches can be sensitive to environmental conditions such as electromagnetic interference. A capable means of avoiding some of these environmental difficulties is to use fiber optic sensors. For example, optical fibers have been configured to break at a minimal stress and have been distributed throughout a structural volume. Damage is sensed when the light passing through a system is interrupted by a severed fiber.[5] However, this technique measures purely effects local to the fiber. Therefore, it requires either a priori knowledge of where the damage is most likely to occur or a dense distribution of fibers throughout the structure, potentially altering the favorable behavior of the structure itself. In addition, once a fiber has been broken, the light is completely interrupted; thus, one cannot determine whether the flaw remains of the same magnitude or is becoming more extensive.

More advanced fiber sensors[6] provide means to more economically collect pointwise data about a structure. For instance, fiber optic Bragg grating sensors[7] can be distributed easily about a structure using only a single fiber. However, this still leaves the necessary task of storing and processing, or inverting, the data.

Here, rather than try to determine the state of a structure, a simple means of determining if a structure has departed from its intended operation is proposed. This paper introduces a structural integrity monitoring approach that utilizes finite-length fiber optic displacement sensors to circumvent many of these difficulties. One way to view this technique is with a null, or balance, sensor in the following manner: For a given structure, sensor paths are determined such that, when their measured effects are combined, they detect an averaged behavior of the perfect structure. Similarly, a second combination of distinctly different paths is calculated that measures the identical averaged behavior. Hence, the measurement of their difference is zero. However, once the structure deviates from its pristine state, the sensor groups display different responses to the in situ changes. At this point, their differential measurement is no longer zero; thus, the sensor becomes unbalanced, indicating damage.

Perhaps the most notable advantage of this approach is that the sensors do not have to be located at or near the site of the damage to detect the loss of integrity of the structure. This volumetric sensing capability results from the use of finite-length measurement paths that integrate local effects over a relatively long path rather than sensors that merely measure effects in a local region. Thus, although this approach does not necessarily determine the location or geometry of a flaw, it provides a means to detect damage throughout a structural volume with only a few sensors. Further, because at most eight sensors are required for simple prismatic structures, a large amount of postprocessing of data is not required. In fact, provided the structure is operating properly, the data from the sensor are null. When the sensor produces a nonzero signal, its magnitude indicates some departure of the structure from its intended operation. Finally, this monitoring technique also includes a measure of the growth of a flaw rather than merely indicating its existence.

II. Measurement Technique

A. Fiber Optic Displacement Sensor

This detection technique utilizes fiber optic displacement sensors as the measurement device. When an optical fiber is placed in a uniaxial strain field aligned with the fiber, light passing through the fiber experiences a phase change proportional to the displacement of the fiber, as given in Eq. (1) (Ref. 8). In this expression, $\bar{\varepsilon}$ is the average strain of the fiber; d is the length of the fiber; and S_f is a constant, depending on the materials of the fiber and the wavelength of the light:

$$\Delta\varphi = S_f \bar{\varepsilon} d \tag{1}$$

Two such fibers can be connected as a Mach–Zender interferometer. Here, a beam of light is split and passed through both fibers and then recombined to produce an interference pattern. The phase difference between the beams of light traversing through two fiber paths of identical materials and length d, is given in Eq. (2) where $\bar{\varepsilon}_1$ and $\bar{\varepsilon}_2$ are the average strain experienced by the two fibers, respectively.[9] For the purpose of this discussion, the fibers with average strain $\bar{\varepsilon}_1$ and $\bar{\varepsilon}_2$ are referred to as the "positive" and "negative" branches of the interferometer, respectively. Similarly, by adding the phase differential between k pairs of fibers, the total phase change can be represented by Eq. (3). Note that Eq. (3) also can be viewed as an equivalent interferometer where the fibers $1, \ldots, k$ are the positive branch and $k+1, \ldots, 2k$ are the negative branch:

$$\Delta\varphi = S_f(\bar{\varepsilon}_1 - \bar{\varepsilon}_2)d \tag{2}$$

$$\Delta\varphi = S_f(\bar{\varepsilon}_1 + \cdots + \bar{\varepsilon}_k - \bar{\varepsilon}_{k+1} - \cdots - \bar{\varepsilon}_{2k})d \tag{3}$$

B. Measurement Path

The average strain experienced by a fiber embedded in a structural volume is dependent on at least two factors: the strain state

---

Received Jan. 27, 1995; revision received May 25, 1995; accepted for publication Dec. 25, 1996.

*Graduate Research Assistant, Department of Aerospace Engineering, FXB Building, 1320 Beal Street.

†Assistant Professor, Department of Aerospace Engineering, FXB Building, 1320 Beal Street.

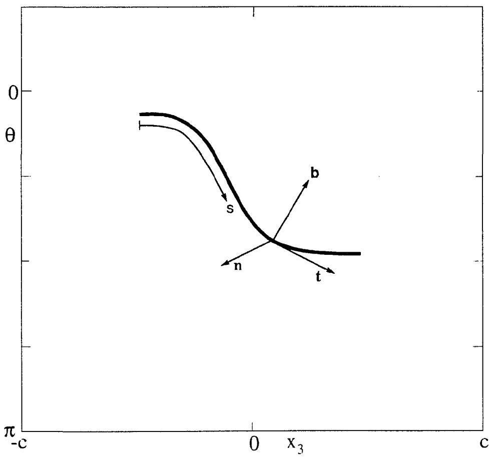

Fig. 1 Direction vectors of an arbitrary sensor path.

of the structure and the path of the fiber through the volume. Consider the arbitrary path shown in Fig. 1. This path $\boldsymbol{p}(s)$ is parametrized in the x_1, x_2, and x_3 directions by the functions $\boldsymbol{p}(s) = \{\zeta_1(s), \zeta_2(s), \zeta_3(s)\}$. Further, the vector tangent to the path, $\boldsymbol{t}$, and the two vectors normal to the path, $\boldsymbol{n}$ and $\boldsymbol{b}$, such that $\boldsymbol{t}, \boldsymbol{n}, \boldsymbol{b}$ form a right-handed orthogonal basis, also are shown. The average strain of this path is given by Eq. (4), where d is the length of the path; $t_i(s)$, $n_i(s)$, and $b_i(s)$ are components of the path vectors; and $\varepsilon_{ij}(x_1, x_2, x_3)$ $(i, j = 1, 2, 3)$ are Cartesian components of the Lagrangian strain tensor. The coefficients C_{ij} describe the sensitivity of the fiber to various strain components; i.e., C_{11}, C_{22}, and C_{33} represent the sensitivity to the tangent, transverse (aligned with the $\boldsymbol{n}$ direction), and transverse (aligned with the $\boldsymbol{b}$ direction) components, respectively[10]:

$$\bar{\varepsilon} = \int_0^d \Bigg\{ \sum_{i=1}^{3} \sum_{j=1}^{3} [C_{11} t_i(s) t_j(s) + C_{12} t_i(s) n_j(s) + C_{13} t_i(s) b_j(s) + C_{21} n_i(s) t_j(s) + C_{22} n_i(s) n_j(s) + C_{23} n_i(s) b_j(s) + C_{31} b_i(s) t_j(s) + C_{32} b_i(s) n_j(s) + C_{33} b_i(s) b_j(s)]\, \varepsilon_{ij}[\zeta_1(s), \zeta_2(s), \zeta_3(s)] \Bigg\}\, \mathrm{d}s \tag{4}$$

Sechler[10] uses a slightly different notation, representing the path in terms of its direction cosines rather than the components of the tangent and normal vectors.

III. Existence of Invariant Paths for All Prismatic Structures Under End Loading

Using the tools presented in the preceding section, we can now develop an in situ structural integrity monitoring technique. The basic concept of this particular technique is to create a series of fiber paths such that, independent of the type of loading on the structure considered, the differential strain between the paths, given by Eq. (3), is zero as long as the structure remains undamaged. Hence, such a path combination can be considered a null sensor. Examples of such damage include cracks or cavities. First, so that a structural integrity monitoring technique be practical, it should be applicable to a broad range of structures. Therefore, this section presents a proof that invariant paths exist for all straight prismatic structures of linear elastic, isotropic, homogeneous materials.

The positive end face of the prismatic cylinder with arbitrary cross section shown in Fig. 2 is loaded by stresses on the positive face. When integrated over the face, these stresses can be modeled as the following resultant forces: two shear forces F_2 and F_3, tension F_1, two bending moments M_2 and M_3, and torsion M_1. All resultant loads act through the centroid of the cross section. In addition, the coordinate frame is aligned with the principal directions of the cross section such that the product of inertia $I_{23} = 0$. The negative end face of the cylinder is subjected to self-equilibrating resultant loads so that the cylinder is in static equilibrium. Further, to show that the sensor is temperature compensated, the cylinder is subjected to a uniform temperature change ΔT. The three-dimensional Lagrangian strain tensor field describing the deformation of the cylinder due to a prescribed resultant end loading is given by Eq. (5) (Ref. 11), where τ is a constant depending on M_1, F_2, and F_3, respectively. In addition, A is the area of the cross section, ν is the Poisson's ratio of the cylinder material, E is the Young's modulus of the cylinder material, α is the coefficient of linear thermal expansion of the material, and I_2 and I_3 are the moments of inertia about the x_2 and x_3 axes, respectively.

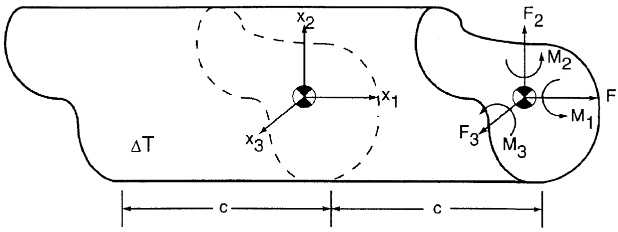

Fig. 2 Prismatic cylinder under resultant end loading.

The functions $\phi(x_2, x_3)$, $\chi_1(x_2, x_3)$, and $\chi_2(x_2, x_3)$ are harmonic solutions to boundary value problems solved over the particular boundary of the given cross section. For a known cross section, specific expressions for $\phi(x_2, x_3)$, $\chi_1(x_2, x_3)$, $\chi_2(x_2, x_3)$, and τ can be determined and substituted into Eq. (5), yielding the infinitesimal strain state throughout the cylinder. Note that this is an exact representation of the strain state if the actual loading is derived from stresses obtained from the Lagrangian strain tensor. However, it is also a representation in the Saint-Venant sense for a loading distributed over the positive end face of the cylinder.[10] Thus any end loading of the cylinder can be broken into its resultant components about the centroid of the cross section and, as long as the sensors are a reasonable distance from the end faces, the preceding expressions are valid. For this proof it is not important that we know the exact form of $\phi(x_2, x_3)$, $\chi_1(x_2, x_3)$, and $\chi_2(x_2, x_3)$, only that we note that they exist and do not vary in the x_1 direction:

$$\begin{aligned}
\varepsilon_{11}(x_1, x_2, x_3) &= \frac{1}{E}\left[\frac{F_1}{A} + \frac{M_2 x_3}{I_2} - \frac{M_3 x_2}{I_3} - \frac{F_2 x_2 (c - x_1)}{I_3} - \frac{F_3 x_3 (c - x_1)}{I_2}\right] + \alpha \Delta T \\
\varepsilon_{22}(x_1, x_2, x_3) &= \frac{\nu}{E}\left[-\frac{F_1}{A} - \frac{M_2 x_3}{I_2} + \frac{M_3 x_2}{I_3} + \frac{F_2 x_2 (c - x_1)}{I_3} + \frac{F_3 x_3 (c - x_1)}{I_2}\right] + \alpha \Delta T \\
\varepsilon_{33}(x_1, x_2, x_3) &= \varepsilon_{22}(x_1, x_2, x_3) \\
\varepsilon_{12}(x_1, x_2, x_3) &= \frac{\tau}{2}\left[-x_3 + \frac{\partial}{\partial x_2}\phi(x_2, x_3)\right] - \frac{F_2}{2EI_3}\left[\frac{\nu}{2}(x_2^2 - x_3^2) + x_3^2 + \frac{\partial}{\partial x_2}\chi_1(x_2, x_3)\right] \\
&\quad - \frac{F_3}{2EI_2}\left[\frac{\partial}{\partial x_2}\chi_2(x_2, x_3) + x_2 x_3 (2 + \nu)\right] \\
\varepsilon_{13}(x_1, x_2, x_3) &= \frac{\tau}{2}\left[-x_2 + \frac{\partial}{\partial x_3}\phi(x_2, x_3)\right] - \frac{F_3}{2EI_2}\left[\frac{\nu}{2}(x_3^2 - x_2^2) + x_2^2 + \frac{\partial}{\partial x_3}\chi_2(x_2, x_3)\right] \\
&\quad - \frac{F_2}{2EI_3}\left[\frac{\partial}{\partial x_3}\chi_1(x_2, x_3) + x_2 x_3 (2 + \nu)\right] \\
\varepsilon_{23}(x_1, x_2, x_3) &= 0
\end{aligned} \tag{5}$$

As an example, one can consider eight sensors of equal length embedded in the cylinder whose paths are defined by the parameterization given in Eq. (6), where $\{\zeta_1(s), \zeta_2(s), \zeta_3(s)\}$ is a set of three arbitrary functions and Δ is an arbitrary constant. Here $\zeta_1(s), \zeta_2(s), \zeta_3(s)$ and Δ are considered as being specified, or data. The paths are derived from these data via Eq. (6). This particular collection of paths is shown to be invariant for all prismatic structures; however, they are not necessarily unique or even optimum for a given application. To prove the invariance of the set $\{\boldsymbol{p}_i(s)\}(i = 1, \ldots, 8)$, we define the vectors associated with path $\boldsymbol{p}_1(s)$ to be as given in Eq. (7) without loss of generality. Further, by scaling t_i, and n_i $(i = 1, 2, 3)$ appropriately, they satisfy the condition that $\boldsymbol{t}$, $\boldsymbol{n}$, and $\boldsymbol{b}$ be orthonormal. The path vectors associated with the other seven sensor paths given in Eq. (6) similarly can be determined to be consistent with the definition in Eq. (7). For example, the corresponding path vectors associated with $\boldsymbol{p}_6(s)$ are shown in Eq. (8):

$$
\begin{gathered}
\boldsymbol{p}_1(s) = \{\zeta_1(s), \zeta_2(s), \zeta_3(s)\} \qquad \boldsymbol{p}_2(s) = \{\zeta_1(s), -\zeta_2(s), -\zeta_3(s)\} \\
\boldsymbol{p}_3(s) = \{-\zeta_1(s), \zeta_2(s), \zeta_3(s)\} \\
\boldsymbol{p}_4(s) = \{-\zeta_1(s), -\zeta_2(s), -\zeta_3(s)\} \\
\boldsymbol{p}_5(s) = \{\zeta_1(s) + \Delta, \zeta_2(s), \zeta_3(s)\} \\
\boldsymbol{p}_6(s) = \{\zeta_1(s) + \Delta, -\zeta_2(s), -\zeta_3(s)\} \\
\boldsymbol{p}_7(s) = \{-\zeta_1(s) - \Delta, \zeta_2(s), \zeta_3(s)\} \\
\boldsymbol{p}_8(s) = \{-\zeta_1(s) - \Delta, -\zeta_2(s), -\zeta_3(s)\}
\end{gathered}
\tag{6}
$$

$$
\begin{aligned}
\boldsymbol{t}^1 &= \{t_1(s), t_2(s), t_3(s)\} \qquad \boldsymbol{n}^1 = \{n_1(s), n_2(s), n_3(s)\} \\
\boldsymbol{b}^1 &= \{t_2(s)n_3(s) - n_2(s)t_3(s), t_3(s)n_1(s) \\
&\quad - n_3(s)t_1(s), t_1(s)n_2(s) - n_1(s)t_2(s)\}
\end{aligned}
\tag{7}
$$

$$
\begin{aligned}
\boldsymbol{t}^6 &= \{t_1(s), -t_2(s), -t_3(s)\} \qquad \boldsymbol{n}^6 = \{n_1(s), -n_2(s), -n_3(s)\} \\
\boldsymbol{b}^6 &= \{t_2(s)n_3(s) - n_2(s)t_3(s), n_3(s)t_1(s) \\
&\quad - t_3(s)n_1(s), n_1(s)t_2(s) - t_1(s)n_2(s)\}
\end{aligned}
\tag{8}
$$

If the sensors are configured such that sensors 1–4 compose the positive branch of the interferometer and sensors 5–8 compose the negative branch, then the differential strain measured by the interferometer, $\bar{\varepsilon}_I$, is presented in Eq. (9). The factor $\operatorname{sgn}(\frac{9}{2} - r)$ ensures that the positive-branch sensors are added whereas the negative-branch sensors are subtracted:

$$
\begin{aligned}
\bar{\varepsilon}_I &= \sum_{n=1}^{4} (\bar{\varepsilon}_n - \bar{\varepsilon}_{n+4}) \\
&= \sum_{r=1}^{8} \sum_{i=1}^{3} \sum_{j=1}^{3} \big[C_{11} t_i^r(s) t_j^r(s) + C_{22} n_i^r(s) n_j^r(s) \\
&\quad + C_{33} b_i^r(s) b_j^r(s) + C_{12} t_i^r(s) n_j^r(s) + C_{13} t_i^r(s) b_j^r(s) \\
&\quad + C_{23} t_i^r(s) n_j^r(s) + C_{21} n_i^r(s) t_j^r(s) + C_{31} b_i^r(s) t_j^r(s) \\
&\quad + C_{32} b_i^r(s) n_j^r(s)\big] \varepsilon_{ij}(\boldsymbol{p}_r(s)) \operatorname{sgn}\left(\frac{9}{2} - r\right)
\end{aligned}
\tag{9}
$$

Substituting the expressions for $\varepsilon_{ij}(x_1, x_2, x_3)$ from Eq. (5), $\boldsymbol{p}_r(s)$ from Eq. (6), and the path vectors, $\boldsymbol{t}^r$, $\boldsymbol{n}^r$, and $\boldsymbol{b}^r$ discussed earlier into Eq. (9) and simplifying yields Eq. (10). Thus, the interferometer is insensitive to the resultant loading considered as long as the cylinder remains within the confines of the analysis. A most notable constraint is that the structure need be prismatic. Because the cross section considered is arbitrary, such invariant paths exist for all homogeneous, isotropic, prismatic structures of linear elastic materials. Note that the choice of paths is not unique because $\{\zeta_1(s), \zeta_2(s), \zeta_3(s_3)\}$ can be varied. Thus, in practice, one could determine the optimal path geometry $\{\zeta_1(s), \zeta_2(s), \zeta(s_3)\}$ with respect to such factors as ease of manufacturing and sensitivity to flaws or restrictions such as not allowing the fibers to intersect. At this point, Eq. (6) can be applied to create a set of invariant paths. Further, although eight sensors are required for the most general cross section, choosing appropriate families of paths to exploit possible symmetries of a given cross section can reduce the number of sensors required to maintain invariance to as few as four:

$$
\bar{\varepsilon}_I = 0 \tag{10}
$$

IV. Example: Monitoring a Prismatic Circular Cylinder

A. Problem Definition

Because of its simple, analytically tractable geometry, a solid prismatic circular cylinder was chosen to demonstrate the applicability and features of this approach. The cylinder of radius a and length c is loaded in tension F_1, as shown in Fig. 3. Note that, for the duration of this example, all parameters are made nondimensional. Pertinent quantities are nondimensionalized as shown in Eq. (11):

$$
\begin{gathered}
\hat{x}_i = x_i / a \qquad \hat{a} = 1 \qquad \hat{c} = c / a \\
\hat{F}_1 = F_1 / E a^2 \qquad \hat{r} = r / a
\end{gathered}
\tag{11}
$$

Because of the relative ease of manufacturing, sensing fibers wound in helical paths are utilized. Equation (12) defines the parameterization of a helical path in terms of the angle traversed by the helix, δ. In addition, Fig. 4 shows the physical representation of the parameters involved: β is the angle of the helix, ϕ is the radial location of the start of the helix, x_h is the starting location of the helix in the x_1 direction, and $\hat{r}$ is the nondimensional radius of the helix. It can be shown, via the method of the preceding section and using the symmetries of the cross section, that the four helical paths given in Eq. (13) are invariant to end loads and a uniform temperature distribution. To produce invariance, $\boldsymbol{p}_1(s)$ and $\boldsymbol{p}_2(s)$ are the positive branch of the interferometer whereas $\boldsymbol{p}_3(s)$ and $\boldsymbol{p}_4(s)$ are the negative branch:

$$
\boldsymbol{p}_h(\delta, \phi, \beta, \hat{r}, \hat{x}_h) = \{\delta \hat{r} \tan\beta + \hat{x}_h, \hat{r}\cos(\delta + \phi), \hat{r}\sin(\delta + \phi)\} \tag{12}
$$

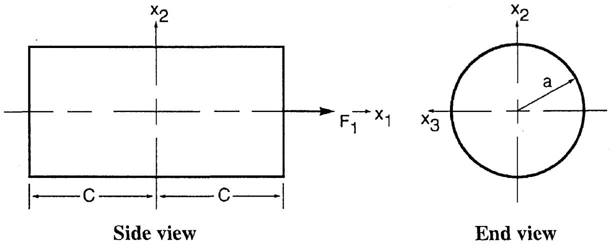

Fig. 3 Prismatic circular cylinder in tension.

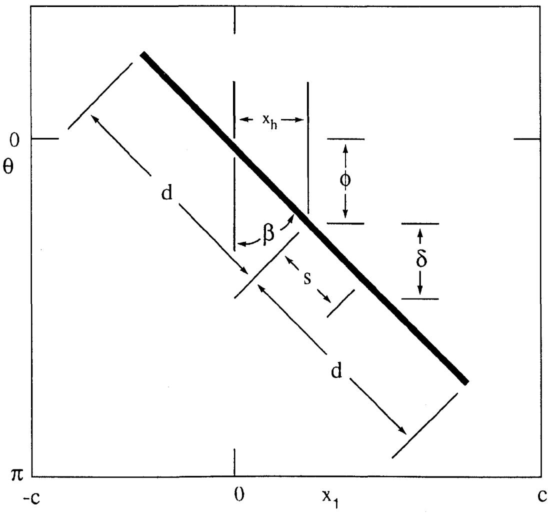

Fig. 4 Parameters of a helical path.

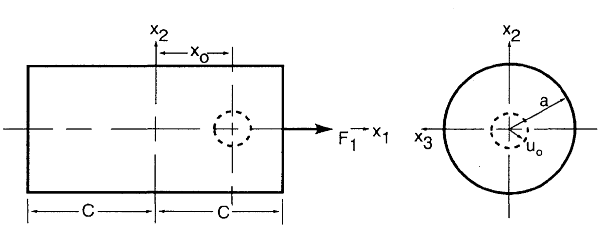

Side view End view

Fig. 5 Prismatic circular cylinder with spherical cavity (hole size greatly exaggerated).

$$p_1(\delta) = p_h(\delta, \phi, \beta, \hat{r}, \hat{x}_h) \qquad p_2(\delta) = p_h(\delta, \phi + \pi, \beta, \hat{r}, \hat{x}_h)$$
$$p_3(\delta) = p_h(\delta, \phi, -\beta, \hat{r}, -\hat{x}_h) \tag{13}$$
$$p_4(\delta) = p_h(\delta, \phi + \pi, -\beta, \hat{r}, -\hat{x}_h)$$

For this example, damage is introduced into the cylinder in the form of a spherical cavity located on the longitudinal x_1 axis as shown in Fig. 5. The hole is fully defined by its radius u_o, and its location on the x_1 axis, x_0. The asymptotic solution of the Lagrangian strain tensor for this cylinder is given by Neuber[12] in Eq. (14), where the radius of the hole is assumed to be much smaller than the radius of the cylinder (i.e., $\hat{u}_o \ll 1$). In Sec. IV.B, the radius of the helix is assumed to be at least one radius of the hole smaller than the radius of the cylinder (i.e., $\hat{r} < 1 - \hat{u}_o$):

$$\begin{aligned}
\varepsilon_{11}(\hat{x}_1, \hat{x}_2, \hat{x}_3) = \frac{1+\nu}{E} \Bigg\{ & \frac{A_T\left(-2\hat{x}_1^2 + \hat{x}_2^2 + \hat{x}_3^2\right)}{\left(\hat{x}_1^2 + \hat{x}_2^2 + \hat{x}_3^2\right)^{\frac{5}{2}}} + \frac{B_T\left[8\hat{x}_1^4 + 3\left(\hat{x}_2^2 + \hat{x}_3^2\right)^2 - 24x_1^2\left(\hat{x}_2^2 + \hat{x}_3^2\right)\right]}{\left(\hat{x}_1^2 + \hat{x}_2^2 + \hat{x}_3^2\right)^{\frac{9}{2}}} \\
& + \frac{C_T\left[2\hat{x}_1^4(4\nu - 5) + \hat{x}_1^2\left(\hat{x}_2^2 + \hat{x}_3^2\right)(4\nu - 7) - 2\left(\hat{x}_2^2 + \hat{x}_3^2\right)^2(2\nu - 1)\right]}{\left(\hat{x}_1^2 + \hat{x}_2^2 + \hat{x}_3^2\right)^{\frac{7}{2}}} \Bigg\} \\
\varepsilon_{22}(\hat{x}_1, \hat{x}_2, \hat{x}_3) = \frac{1+\nu}{E} \Bigg\{ & \frac{A_T\left[-2\hat{x}_2^4 + \hat{x}_3^4 + \hat{x}_1^2\left(\hat{x}_2^2 + \hat{x}_3^2\right) - \hat{x}_2^2\hat{x}_3^2\right]}{\left(\hat{x}_2^2 + \hat{x}_3^2\right)\left(\hat{x}_1^2 + \hat{x}_2^2 + \hat{x}_3^2\right)^{\frac{5}{2}}} + \frac{3B_T\left[-4\left(\hat{x}_1^4 + \hat{x}_2^4\right) + \hat{x}_3^4 + 27\hat{x}_1^2\hat{x}_2^2 - 3\hat{x}_3^2\left(\hat{x}_1^2 + \hat{x}_2^2\right)\right]}{\left(\hat{x}_1^2 + \hat{x}_2^2 + \hat{x}_3^2\right)^{\frac{9}{2}}} \\
& + \frac{3C_T\hat{x}_1^2}{\left(\hat{x}_1^2 + \hat{x}_2^2 + \hat{x}_3^2\right)^{\frac{5}{2}}} - \frac{15C_T\hat{x}_1^2\hat{x}_2^2}{\left(\hat{x}_1^2 + \hat{x}_2^2 + \hat{x}_3^2\right)^{\frac{7}{2}}} \Bigg\} \\
\varepsilon_{33}(\hat{x}_1, \hat{x}_2, \hat{x}_3) = \frac{1+\nu}{E} \Bigg\{ & \frac{A_T\left[-2\hat{x}_3^4 + \hat{x}_2^4 + \hat{x}_1^2\left(\hat{x}_2^2 + \hat{x}_3^2\right) - \hat{x}_2^2\hat{x}_3^2\right]}{\left(\hat{x}_2^2 + \hat{x}_3^2\right)\left(\hat{x}_1^2 + \hat{x}_2^2 + \hat{x}_3^2\right)^{\frac{5}{2}}} + \frac{3B_T\left[-4\left(x_1^4 + x_3^4\right) + x_2^4 + 27x_1^2x_3^2 - 3x_2^2\left(x_1^2 + x_2^2\right)\right]}{\left(\hat{x}_1^2 + \hat{x}_2^2 + \hat{x}_3^2\right)^{\frac{9}{2}}} \\
& + \frac{3C_T\hat{x}_1^2}{\left(\hat{x}_1^2 + \hat{x}_2^2 + \hat{x}_3^2\right)^{\frac{5}{2}}} - \frac{15C_T\hat{x}_1^2\hat{x}_3^2}{\left(\hat{x}_1^2 + \hat{x}_2^2 + \hat{x}_3^2\right)^{\frac{7}{2}}} \Bigg\} \\
\varepsilon_{12}(\hat{x}_1, \hat{x}_2, \hat{x}_3) = \frac{1+\nu}{E} & \left[\frac{-3\hat{x}_1\hat{x}_2(A_T - 2\nu C_T)}{\left(\hat{x}_1^2 + \hat{x}_2^2 + \hat{x}_3^2\right)^{\frac{5}{2}}} - \frac{15C_T\hat{x}_1^3\hat{x}_2}{\left(\hat{x}_1^2 + \hat{x}_2^2 + \hat{x}_3^2\right)^{\frac{7}{2}}} + \frac{5B_T\hat{x}_1\hat{x}_2\left(4\hat{x}_1^2 - 3\hat{x}_2^2 - 3\hat{x}_3^2\right)}{\left(\hat{x}_1^2 + \hat{x}_2^2 + \hat{x}_3^2\right)^{\frac{9}{2}}} \right] \\
\varepsilon_{13}(\hat{x}_1, \hat{x}_2, \hat{x}_3) = \frac{1+\nu}{E} & \left[\frac{-3\hat{x}_1\hat{x}_3(A_T - 2\nu C_T)}{\left(\hat{x}_1^2 + \hat{x}_2^2 + \hat{x}_3^2\right)^{\frac{5}{2}}} - \frac{15C_T\hat{x}_1^3\hat{x}_3}{\left(\hat{x}_1^2 + \hat{x}_2^2 + \hat{x}_3^2\right)^{\frac{7}{2}}} + \frac{5B_T\hat{x}_1\hat{x}_3\left(4\hat{x}_1^2 - 3\hat{x}_2^2 - 3\hat{x}_3^2\right)}{\left(\hat{x}_1^2 + \hat{x}_2^2 + \hat{x}_3^2\right)^{\frac{9}{2}}} \right] \\
\varepsilon_{23}(\hat{x}_1, \hat{x}_2, \hat{x}_3) = \frac{1+\nu}{E} & \left[\frac{-3\hat{x}_2\hat{x}_3A_T}{\left(\hat{x}_1^2 + \hat{x}_2^2 + \hat{x}_3^2\right)^{\frac{5}{2}}} + \frac{15B_T\hat{x}_2\hat{x}_3\left(6\hat{x}_1^2 - \hat{x}_2^2 - \hat{x}_3^2\right)}{\left(\hat{x}_1^2 + \hat{x}_2^2 + \hat{x}_3^2\right)^{\frac{9}{2}}} - \frac{15C_T\hat{x}_1^2\hat{x}_2\hat{x}_3}{\left(\hat{x}_1^2 + \hat{x}_2^2 + \hat{x}_3^2\right)^{\frac{7}{2}}} \right] \\
A_T = \frac{-\hat{F}_1\hat{u}_o^3(6 - 5\nu)}{2\pi(7 - 5\nu)}, \quad & B_T = \frac{\hat{F}_1\hat{u}_o^5}{2\pi(7 - 5\nu)}, \quad C_T = \frac{5\hat{F}_1\hat{u}_o^3}{2\pi(7 - 5\nu)}
\end{aligned} \tag{14}$$

Figure 6 shows the axial strain ϵ_{11}, contours in $x_1 - x_3$ plane around the void. Regions 1 and 3 are in tension, whereas regions 2 and 4 are in compression. The shape of the contours change as the distance from the hole increases. It is useful to identify regions close to the hole and far from the hole. The dashed line represents an approximate boundary between the near-field and the far-field strain regions. This boundary is defined by a change in the qualitative behavior of sensors in the two regions. In short, if the flaw occurs close enough to a helical path such that part of the sensing fiber is within the near-field region, the sensor output will be shown to have a behavior distinct from one detecting a hole purely in the far-field region.

The response of a sensor aligned with the x_1 axis and assumed to be infinitesimal so that the strain is constant along the path length is shown in Fig. 7. This sensor lies in the near-field region of the hole. Here, ε_{11}^o is the strain in the undamaged cylinder and $\hat{x}_\Delta$ is the distance between the start of the helical sensor and the center of the flaw (i.e., $\hat{x}_\Delta = \hat{x}_o - \hat{x}_h$). In contrast, the response of an infinitesimal sensor, once again aligned with the x_1 axis, but located in the far-field region, is shown in Fig. 8. Note the scale difference between the two plots. The near-field sensor measures the largest difference in strain from the undamaged state when the flaw is closest to the sensor (i.e., $\hat{x}_\Delta = 0$). However, the far-field sensor experiences no difference in strain from the undamaged case at $\hat{x}_\Delta = 0$, but instead detects a maximum difference at locations offset from the flaw. Because one of the strengths of this structural integrity monitoring technique is that it does not rely on sensors being close to the damage to detect flaws, this different behavior of sensors in the far-field region becomes important and will affect the later results. For comparison, these same regions of qualitative strain behavior can be shown to exist for the two-dimensional case of a plate with a circular hole.[13]

B. Detection Results

Substituting the strain components from Eq. (14) and the helical parameterization of Eq. (13) into Eq. (4) and integrating yields the average strain of a helical path, as given in Eq. (15). The assumption

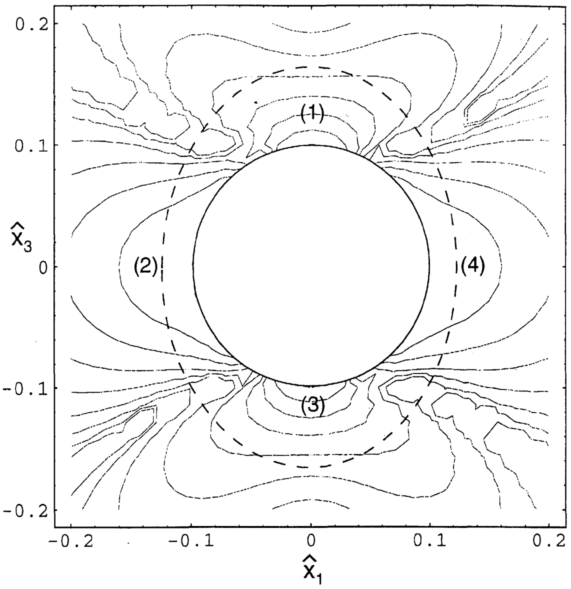

Fig. 6 **The ε_{11} contours surrounding void in the x_1-x_3 plane ($\hat{u}_o$ = 0.1) (inside the dotted line is approximately the near-field region, whereas outside is the far-field region).**

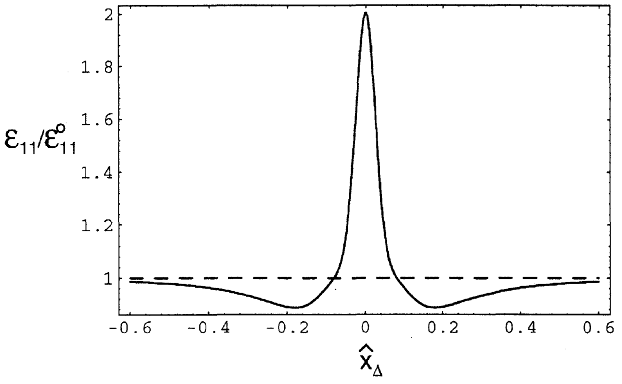

Fig. 7 **Sensor response in near-field region ($\hat{u}_o$ = 0.1, $\hat{r}$ = 0.11).**

is made that the length of the helix is much greater than the hole radius (i.e., $\hat{d}_h \gg \hat{u}_o$). In addition, because the coefficients C_{ij} $(i \neq j)$ are typically orders of magnitude less than the coefficients C_{ij} $(i = j)$ (Ref. 14), they are neglected in Eq. (15) to simplify the integration. Including these coefficients would still preserve the invariance of the paths when no damage is present while changing the magnitude of the average strain insignificantly after a cavity forms:

$$
\begin{aligned}
\bar{\varepsilon}_h = {} & \frac{\hat{F}_1}{\pi}(\sin^2\beta + \nu\cos^2\beta) + \frac{\hat{F}_1\hat{u}_o^3(1+\nu)}{2\pi(7-5\nu)\hat{r}^3\tan\beta}\Bigg\{(5\nu-1) \\
& \times \left(C_{11}\cos^2\beta + C_{22}\sin^2\beta - C_{33}\right) \\
& + \frac{\hat{x}_\Delta}{2\left(\hat{r}^2+\hat{x}_\Delta^2\right)^{\frac{7}{2}}}\left[(C_{11}+C_{22})\left(2\hat{r}^6 + 10\nu\hat{r}^6\right.\right. \\
& - 12\hat{r}^4u_o^2 - 10\hat{r}^4x_\Delta^2 + 15\nu\hat{r}^4\hat{x}_\Delta^2 + 3\hat{r}^2\hat{u}_o^2\hat{x}_\Delta^2 \\
& \left. - 11\hat{r}^2\hat{x}_\Delta^4 + \hat{x}_\Delta^6 - 5\nu\hat{x}_\Delta^6\right) \\
& + \cos 2\beta(C_{11}-C_{22})\left(10\hat{r}^6 - 20\nu\hat{r}^6 + 6\hat{r}^4\hat{u}_o^2 + 36\hat{r}^4\hat{x}_\Delta^2\right. \\
& \left. - 45\nu\hat{r}^4\hat{x}_\Delta^2 - 9\hat{r}^2\hat{u}_o^2\hat{x}_\Delta^2 + 27\hat{r}^2\hat{x}_\Delta^4 - 30\nu\hat{r}^2\hat{x}_\Delta^4 + \hat{x}_\Delta^6 - 5\nu\hat{x}_\Delta^6\right) \\
& - 2C_{33}\left(-12\hat{r}^6 + 10\nu\hat{r}^6 + 12\hat{r}^4\hat{u}_o^2 - 10\hat{r}^4\hat{x}_\Delta^2 + 25\nu\hat{r}^4\hat{x}_\Delta^2\right. \\
& \left.\left. - 3\hat{r}^2\hat{u}_o^2\hat{x}_\Delta^2 + \hat{r}^2\hat{x}_\Delta^4 + 20\nu\hat{r}^2\hat{x}_\Delta^4 - \hat{x}_\Delta^6 + 5\nu\hat{x}_\Delta^6\right)\right]\Bigg\} \qquad (15)
\end{aligned}
$$

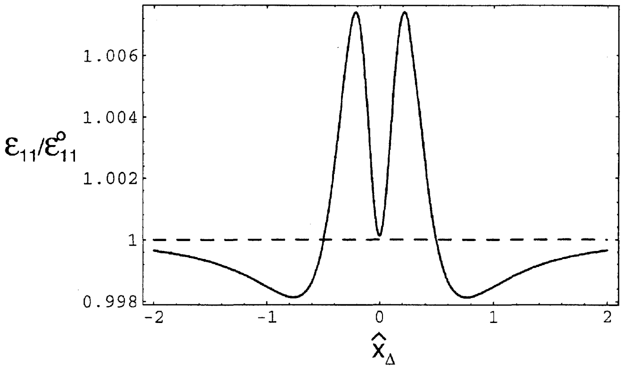

Fig. 8 **Sensor response in far-field region ($\hat{u}_o$ = 0.1, $\hat{r}$ = 0.4).**

Evaluating the average strain for each of the four helical paths given in Eq. (13) and substituting these expressions into Eq. (3) reveals that, when a cavity is present (i.e., $\hat{u}_o \neq 0$), the phase differential between the positive and the negative branches of the interferometer differs from zero except for a few distinct cases. For a fixed tension applied to the cylinder, this phase differential becomes a function of the radius and location of the cavity.

Figure 9 shows the interferometer phase imbalance for the set of helical paths given in Eq. (1) with various void radii; $\hat{x}_o$ is the axial location of the spherical hole and $\hat{r}$ is the radius of the helix. The cylinder is composed of steel with a 4.58-cm in diameter and a 10-kN load applied in tension. Once again, note the scale differences between the plots.

In cases A and B, the radius of the helix is relatively small so that the section of the helix closest to the flaw passes through the near-field strain region. In contrast, in cases C and D, the radius is relatively large so that all of the helixes are entirely within the far-field strain region of the flaw. In all instances, when the spherical hole is more than one radius away from the start of the helixes $(|\hat{x}_o| > 1)$, the qualitative behavior of the interferometer is the same. At $\hat{x}_o \ll -1$, the phase change asymptotes to a negative value; whereas at $\hat{x}_o \gg 1$, the phase change asymptotes to a positive value of the same magnitude. Therefore, the only occasions at which the sensor would not detect flaw occur within the region $|\hat{x}_o| < 1$.

When a helix passes through the near-field strain region of the flaw, the sensor is unable to detect the flaw only at $\hat{x}_o = 0$. However, when the helixes are completely contained within the far-field strain region of the flaw, the sensor is unable to detect the flaw at $\hat{x}_o = 0$ and two other locations. This ambiguity could be relieved through utilizing two sets of four helixes, offset from one another on the x_1 axis by at least one radius of the cylinder. Therefore, if the flaw occurs within $|\hat{x}_o| < 1$ for one group of helixes, it will be at $|\hat{x}_o| > 1$ for the other set and thus at least one sensor will detect flaws occurring anywhere along the x_1 axis. Further, the magnitude of the phase imbalance becomes larger as the radius of the spherical cavity grows; thus, this technique can monitor the proportional growth of the flaw (i.e., preserving the shape of the flaw) provided its geometry is known. Finally, this technique is not sensitive to prismatic alterations to the structure; however, for all intensive purposes, such prismatic flaws do not occur, or are pathological, in actual structures.

V. Further Discussion

Although both the proof of existence of invariant paths outlined in Sec. III and the example presented in Sec. IV considered structures of isotropic, homogeneous material, the mathematical framework of this technique is not limited to such structures. In fact, the flexibility of this technique lies in its ability to exploit symmetries, both material and geometric, that exist for a large class of pristine structures. Restricting oneself to monitoring prismatic structures is just one method to ensure that such symmetries exist. Thus, it is certainly conceivable that structures with other forms of symmetry, such as bodies of revolution or structures with planes of symmetry, also could be embedded with fiber sensor paths that are invariant to loading.

Further, such properties exist for a large group of anisotropic structures. For example, symmetric laminated composites conceiv-

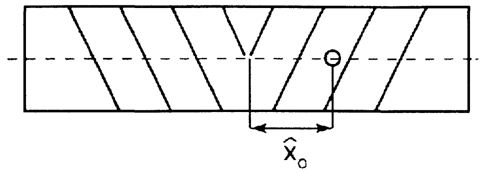

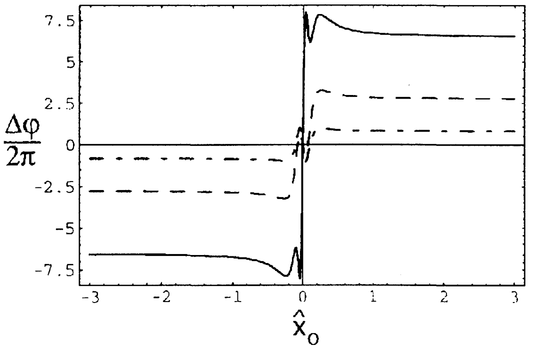

a) $\hat{r} = 0.1$

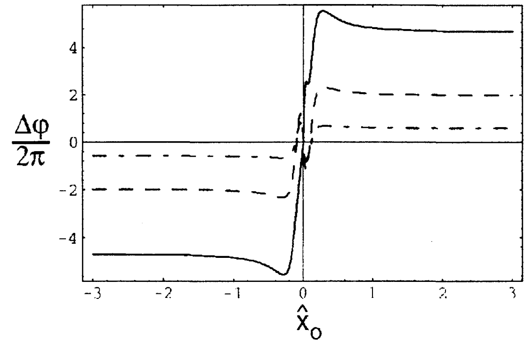

b) $\hat{r} = 0.112$

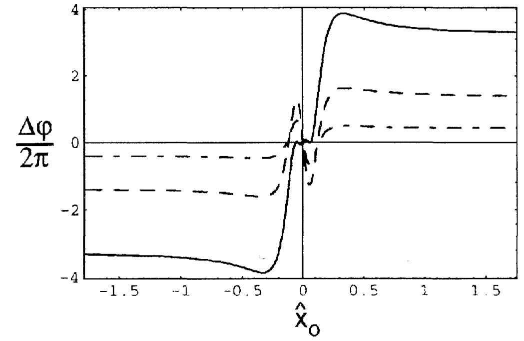

c) $\hat{r} = 0.126$

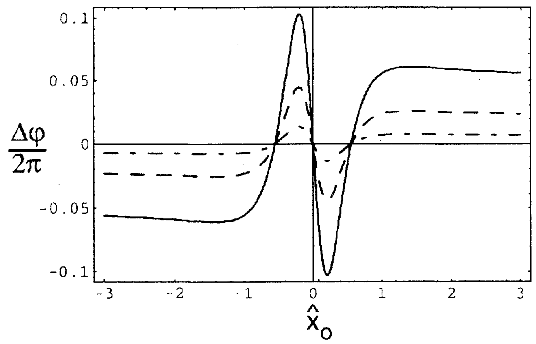

d) $\hat{r} = 0.5$

Fig. 9 Phase imbalance of interferometer for various hole radii ($C_{11} = 1, C_{22} = C_{33} = 0.1, \phi = 0, \beta = \pi/8, \hat{x}_h = 0, S_f = 1.12 \times 10^7/\mathrm{m}$); in a and b, sensors pass through the near-field region, and in c and d, sensors pass through the far-field region only: ——, $\hat{u}_o = 0.1$; – – –, $\hat{u}_o = 0.075$; and – - –, $\hat{u}_o = 0.05$.

ably lend themselves to this method. Although an appropriate numerical technique may be required to pursue this further, because exact pointwise descriptions of the strain state of laminate composites typically are not available, one can envision producing invariant fiber sensors through groups reflected about the midplane. Hence, the approach to monitoring prismatic, isotropic, homogeneous structures presented in this paper is merely a starting point for the monitoring of a broader class of structures.

VI. Conclusions

An in situ structural integrity monitoring technique is described that can detect the presence of nonprismatic flaws in any prismatic structure of isotropic, homogeneous material. This technique utilizes finite-length fiber optic displacement sensors collected into two sets of sensing devices. The relative response of one collection to the other is then measured, in effect detecting the balance of two sets. This balance sensor is insensitive to all end loading as long as the structure remains pristine. However, once a flaw occurs, the detector becomes unbalanced, thus indicating damage without requiring a large amount of postprocessing of data. At the cost of not indicating the geometry or location of the flaw, this detection technique monitors an entire structural volume with only a few sensors because the sensors do not have to be located at or near the site of damage. In addition, a method to determine appropriate sensing paths for all prismatic structures also is presented.

Further, as an example, the monitoring of a circular cylinder with a spherical inclusion on the longitudinal axis is analyzed. Through the use of four sensors arranged in helical paths, the technique detected flaws at all locations except for a few discrete points. However, this deficiency could be corrected through adding four additional helical sensors. Thus this technique can monitor the presence and growth of all flaws considered in the example. Finally, possible extensions of this method to anisotropic and nonhomogeneous materials also are discussed.

Acknowledgments

The support of the Advanced Products Research Agency through Grant F49620-94-1-0472 and the National Science Foundation through Grant CMS 9415328 is gratefully acknowledged.

References

[1] Atluri, S. N., Sampath, S. G., and Tong, P. (eds.), *Structural Integrity of Aging Airplanes*, Springer–Verlag, Berlin, 1991, pp. 1–13.

[2] Kaouk, M., and Zimmerman, D. C., "Structural Damage Assessment Using a Generalized Minimum Rank Perturbation Theory," *AIAA Journal*, Vol. 32, No. 4, 1994, pp. 836–842.

[3] Lim, T. W., and Kashangaki, T. A. L., "Structural Damage Detection of Space Truss Structures Using Best Achievable Eigenvectors," *AIAA Journal*, Vol. 32, No. 5, 1994, pp. 1049–1057.

[4] Manning, R. A., "Structural Damage Detection Using Active Members and Neural Networks," *AIAA Journal*, Vol. 32, No. 6, 1994, pp. 1331–1333.

[5] Collacott, R. A., *Structural Integrity Monitoring*, Chapman and Hall, New York, 1985, pp. 138, 139.

[6] Murphy, K. A., Miller, M. S., Vengsarkar, A. M., and Claus, R. O., "Elliptical-Core, Dual-Mode, Optical Fiber Sensors for Composite Material Laminates," *Journal of Composite Technology and Research*, Vol. 13, 1991, pp. 29–35.

[7] Meltz, G., Morey, W. W., and Glenn, W. H., "Formation of Bragg Grating in Optical Fibers by a Transverse Holographic Method," *Optics Letters*, Vol. 14, 1989, pp. 823–825.

[8] Butter, C. D., and Hocker, G. B., "Fiber Optics Strain Gauge," *Applied Optics*, Vol. 17, No. 18, 1978, pp. 2867–2869.

[9] Washabaugh, P. D., "A Precision Six-Load Component Transducer: A Design Incorporating Finite Length Measurement Paths," *Experimental Mechanics*, Vol. 4, Dec. 1993, pp. 326–335.

[10] Sechler, E., *Elasticity in Engineering*, Dover, New York, 1952, Chap. 4, Sec. 5.

[11] Sokolnikoff, I. S., *Mathematical Theory of Elasticity*, 2nd ed., Krieger, Malabar, FL, 1983, pp. 91–244.

[12] Neuber, H., *Theory of Notch Stresses*, J. W. Edwards, Ann Arbor, MI, 1946, pp. 76–127.

[13] Barber, J. R., *Elasticity*, Kluwer Academic, Norwell, MA, 1992, pp. 92–95.

[14] Dally, W., and Riley, W. F., *Experimental Stress Analysis*, 2nd ed., McGraw–Hill, New York, 1978, pp. 169–173.

R. K. Kapania
Associate Editor